LAWRENCE
LIVERMORE
NATIONAL
LABORATORY

LLNL-JRNL-832880

3D Printed Carbon Aerogels for Polymer-Electrolyte Fuel Cells

A. D. Santamaria, S. Chandrasekaran, O. Philbrick, M. A. Worsley

March 16, 2022

ECS Transactions

Disclaimer

3D Printed Carbon Aerogels for Polymer-Electrolyte Fuel Cells

A. D. Santamaria[1], S. Chandrasekaran[2], O. Philbrick[1], M. Worsley[2]

[1]Department of Mechanical Engineering, Western New England University, Springfield, MA 01119, USA

[2]High Performance Materials Group, Lawrence Livermore National Laboratory, Livermore, CA 94550-9234, USA

Carbon aerogels (CA) are known for ultra-low density, very high surface area, fine porous structure, and excellent electrical conductivity. Recent advances in high resolution 3D printing at LLNL enable the manufacturing of complex structured CA electrodes which have been demonstrated in electrolysis, flow battery, and supercapacitor applications. Polymer-electrolyte fuel cells (PEFC) may be an excellent candidate for these materials/methods as designers seek to optimize membrane-electrode assemblies to achieve higher efficiencies. A major challenge to PEFC design is two-phase flow due to water production which causes pore flooding and leads to cell instability and degradation. To mitigate these effects, groups have investigated the creation of liquid specific pathways in the porous layers to alleviate liquid buildup and enhance gas diffusion. While some progress has been made, traditionally manufactured GDLs, which consist of randomly distributed carbon fibers, are limiting. 3D printed CAs are a promising solution as complex macroporous electrode structures can be manufactured out of micro and nano porous filaments with a high level of control. Additionally, the process may allow for the consolidation of multiple layers (MPL, GDL, & flow channels) into a single printed architecture. In this work various CA lattice structures were printed using a direct ink write (DIW) method and liquid breakthrough pressures were measured to demonstrate the ability to tune the water pathways to achieve specific pressure thresholds. A discussion of the prospects for printed CA electrodes in PEFC will focus on material properties, synthesis techniques, and current challenges.

Introduction

Advances in high resolution 3D printing and carbon aerogel (CA) synthesis are pushing the boundaries of structured electrode design for energy conversion and storage systems [1, 2]. While these new approaches continue to be demonstrated in single-phase electrochemical cells, there is a large opportunity to utilize them in the optimization of multiphase systems such as electrolysis and polymer-electrolyte fuel cells (PEFC). Current PEFC membrane-electrode assemblies (MEA) are multilayer architectures consisting of an ionomer membrane, catalyst layer, and diffusion media all sandwiched

between flow-field reactant channels. Liquid water management in these porous structures is a challenge as flooding reduces gas diffusion rates while dry conditions increase ionic resistance [3-5]. Recently, groups have proposed controlling liquid saturation by developing drainage pathways within the MEA using hydrophobicity and pore gradients as well as various sized perforations. While CA for PEFC have been probed in the past, 3D printed CAs opens new frontiers toward accomplishing these goals by enabling control of morphology and material properties [6]. This work outlines the general 3D printing and CA synthesis process, highlights key two-phase flow considerations, and introduces the prospects for utilization in PEFC, including novel MEA architectures, that these methods may enable.

Two-phase Flow

Liquid-gas two-phase flow management is a primary challenge for PEFC electrode design. Water is formed in the cathode catalyst layer (cCL) as a product of the oxygen reduction reaction (ORR). Some cCL water may back diffuse into the membrane (a process opposed by electroosmotic drag from the anode) while most travels through the cathode side MPL and GDL where it is then removed via flow channels. When the local partial pressure of water exceeds the saturation pressure, water condenses and may distribute throughout pores and reactant channels as droplets, films, and slugs [7]. This two-phase environment leads to complex flow dynamics and, if unmanaged, may have deleterious effects on cell performance [8]. Water buildup within the cCL can reduce the effective active area by blocking key catalyst sites. Additionally, liquid saturation of pores leads to reduced gas diffusion. Within the MPL and GDL liquid transport is dominated by surface tension and viscous effects [9]. Since the velocity of water in the GDL is low, liquid percolation into these porous structures takes place in the capillary fingering regime. Capillary fingering is characterized by the formation of a network of liquid columns and branches [10, 11]. Drainage occurs, and is sustained, when the liquid pressure exceeds the capillary pressure of the porous media. Capillary pressure, p_c, is defined by the Young-Laplace equation:

$$p_c = p_l - p_g = \frac{-2\sigma cos\,(\theta)}{r} \qquad \text{Eq. 1}$$

where p_l is the liquid phase pressure, p_g is the gas phase pressure, σ is the surface tension, θ is the liquid contact angle, and r is the droplet radius. Liquid phase has been shown to preferentially fill larger pores first. In several efforts, small holes were made in the MPL and or GDL to establish liquid pathways for water to transit [12, 13]. Capillary driven flow is affected by adjusting hydrophobicity and or pore size & structure. Smaller radius droplets, for example, have a higher liquid pressure; therefore, they tend to be absorbed into larger droplets they encounter. To this end, several groups have proposed pore gradient structured GDL. Recently, Bazylak's group has explored transverse pore gradients for enhanced liquid drainage [14]. Using an electrospinning method, a bi-layer GDL was manufactured having two distinct porosities: the catalyst interfacing layer consisted of an average pore diameter of ~175 nm while the channel interface layer average pore diameter was ~687 nm. X-ray radiography showed that liquid water content was reduced in the bi-layer GDL compared to a traditional GDL. While promising, this approach was limited to a single step-difference in porosity. 3D-printed lattices could extend this idea by enabling a range of gradients and macropore sizes [15].

3D Printed Carbon Aerogels

CAs are highly porous (> 95%) solid materials known for their very low density, high surface area, high electrical conductivity, thermal and chemical robustness, ultrafine open pore structure, and good mechanical properties [16]. First synthesized in the 1930's, they have been recently demonstrated as electrodes in flow battery, supercapacitor, and electrolyzer systems. CAs are created by replacing the liquid phase of a wet gel with gas, resulting in a porous solid. Traditional CA synthesis follows the sol-gel process:

1.) Polymers, such as commonly used resorcinol-formaldehyde (RF), are mixed with water as well as a catalyst, to form a solution.
2.) During the condensation phase, polymer chains link together into continuous networks forming a gel.
3.) The resulting wet gel is now ready to be dehydrated using either supercritical or subcritical drying techniques which preserve the fine pore structure which may be damaged by liquid surface tension.
4.) Once dried, the aerogel is carbonized in an oven at high temperature producing the final CA.

While there are several types of CAs, this work will focus on a graphene-based material due to its recent success in energy storage applications. For PEFC, the resulting multi-scale pore structures facilitate liquid uptake as well as gas diffusion as demonstrated in Figure 1.

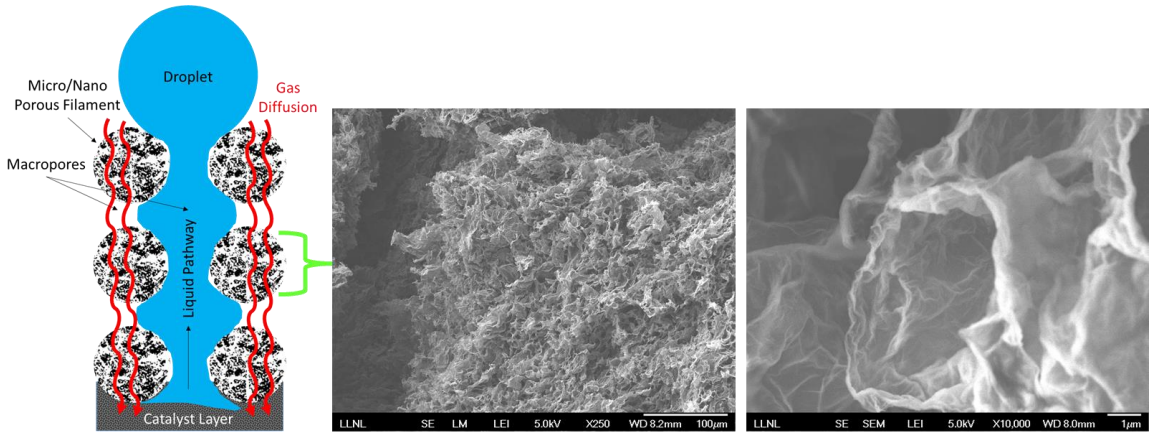

Figure 1. (Left) Proposed two-phase mass transport in PEFC electrode using a CA GDL lattice. (Right) SEM images of the filament's high surface area porous morphology.

3D printed CAs have been demonstrated for a wide range of applications and are of interest as they represent the use of 3D printing to create functional materials [16]. While the aerogel pore morphology is random, structured macroporous features can be formed during the printing process. While two printing methods, direct ink writing (DIW) and stereolithography (SW) are typically used, this work focuses on the DIW process which has sufficient resolution for GDL structures. The following examines the liquid pressure necessary for breakthrough in DIW manufactured GDL lattices and compares them to a traditional GDL paper & cloth. Also, the tunability of 3D printed CAs for liquid transport

is demonstrated by examining the effect of different printed lattice dimensions on breakthrough pressure.

Experimental Methods

Sample Preparation

Graphene oxide (GO), considered affordable and widely available, was used as a precursor to a RF sol–gel ink due to the materials desirable electrical and morphological properties [16]. DIW printing, summarized in Figure 2, utilizes a position-controlled nozzle to extrude ink filaments used to construct 3D structures. Inks for these systems must be thixotropic, that is, they flow under an applied shear stress while returning to a self-supporting solid when the stress is removed [16]. Tuning the viscoelasticity of these non-newtonian fluids is a primary design goal and usually achieved using viscosifiers such as hydrophilic fumed silica powders. Aerogel inks must remain wet both during and after the printing process to ensure proper gelation. This is required so that the liquid from the wet gel can be removed by either freeze-drying or supercritical drying to avoid pore collapse due to capillary forces present during ambient drying [16]. Therefore, print duration must be considered as well as the use of solvents to reduce ink particle agglomeration. During preparation, inks are loaded into a syringe and gas bubbles are removed using a centrifuge to ensure a continuous extrudate. A piston is loaded on top of the ink and gas pressure is applied to control flow rate. The printing speed is adjusted based on the nozzle diameter and ink properties. For current DIW CA printing, filament diameters as small as 200 μm are possible. Figure 3 shows the lattices created using DIW for this work. The lattices for this study are simple cubic cell (SCC) structures. The spacing between the filaments (or ligaments) can be tuned to provide adequate macropores for liquid drainage. Once the printing is complete, the structure is frozen, whereby ice crystallization forms what will be the eventual void space in the carbon filaments. The ice is removed using either the freeze-drying or supercritical drying method leaving behind the highly porous CA.

For this work two separate GO based SCC lattices were printed:

1.) A *fine* lattice structure using the 200 μm nozzle diameter with 400 μm center-to-center ligament distance. Overall thickness was ~1 mm.
2.) A *rough* lattice structure using the 400 μm nozzle diameter with 800 μm center-to-center ligament distance. Overall thickness was ~1.2 mm.

The actual lattice dimensions change significantly after carbonization and so the samples were measured postprocessing using an optical microscope. Table 1 contains key dimensions. The Toray 120 with 5% PTFE wetproofing as well as ELAT carbon cloth were also included for comparison and are used as a benchmark in later testing.

TABLE I: Sample properties.

Sample	Nominal Pore Diameter	Specified Porosity	Thickness	Ligament or Fiber Dia.	Contact Angle
Rough Lattice	~351 μm	>95%	~1000 μm	400 μm	~145°
Fine Lattice	~146 μm	>95%	~1000 μm	200 μm	~145°
Toray 120 5%	~25 μm [17]	78%	370 μm	~10 μm	~145°
ELAT Cloth	~71.2 μm [18]	80%	406 μm	~10 μm	~148°

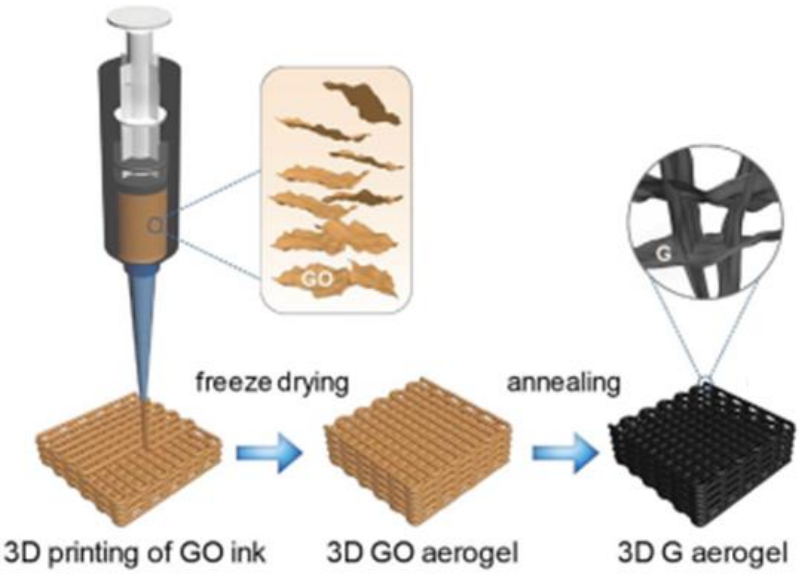

Figure 2. DIW manufacturing process using GO RF sol-gel [19].

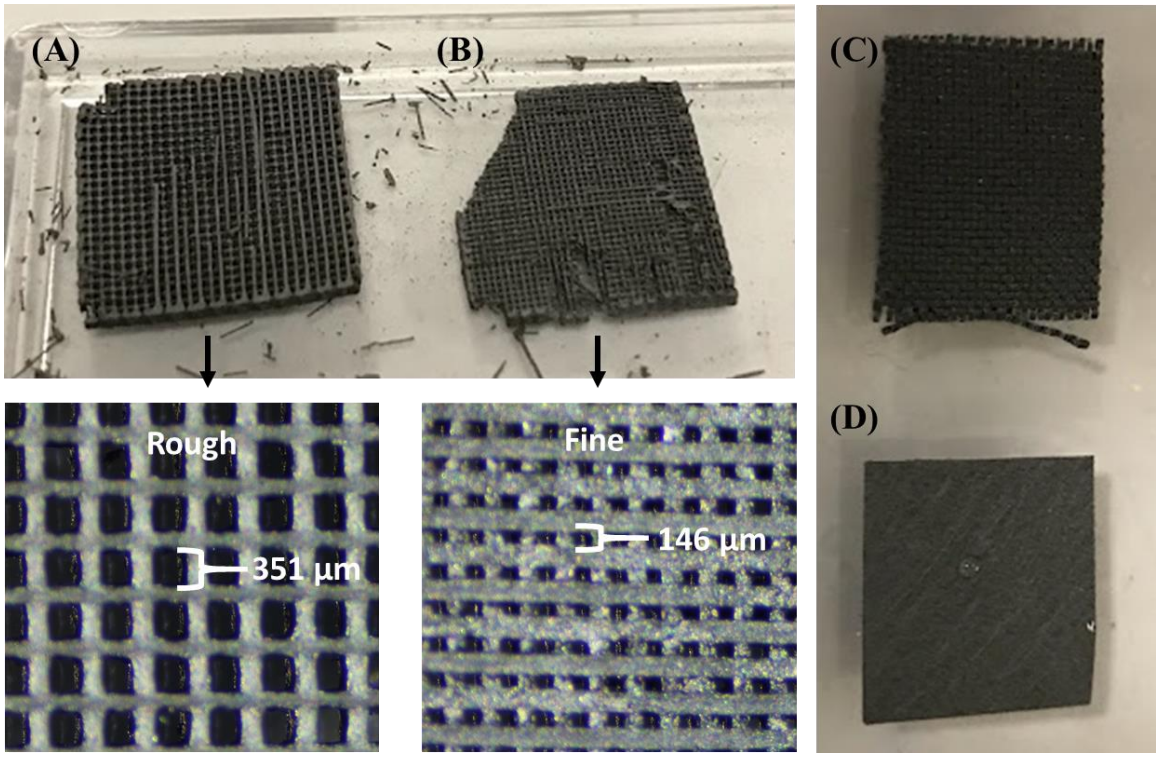

Figure 3. Test samples: (A) Rough lattice (B) Fine lattice (C) ELAT Cloth (D) Toray 120. Gap dimensions were estimated using an optical microscope. Note: Lattice sample images were taken post testing and handling; some damage occurred.

Test Setup & Data Analysis

Liquid breakthrough pressure is considered a gauge of a GDL's barrier to liquid drainage [9]. The ability to tune the breakthrough pressure of a GDL may be useful to liquid management. Breakthrough pressure was measured using a basic liquid injection stage outlined in Figure 4. ~2 cm x 2 cm samples were placed on a gasket and secured using a compression plate (minimum compression was used only to prevent water leakage from the interface). Liquid water was injected through the bottom stage and gasket and into the sample via a ~700 µm through hole at a rate of 2000 µL/hr using a digital syringe pump (NE-300). Liquid pressure was measured at 10 Hz using an Omega transducer and recorded in LabView. Breakthrough pressure curves for all samples are displayed in Figure 4. Upon injection the pressure climbs due to water being forced into GDL pores; the slope can be attributed to the expansion of the injection system, mostly the tubing, and matches behavior reported in previous studies [9]. At some point the pressure reaches a maximum which is accompanied by droplet formation on the sample surface. This maximum pressure is recorded as the breakthrough pressure. The pressure signal then falls as it is relieved via drainage to the surface droplet. The pressure remains elevated after breakthrough due to viscous effects from the continued injection.

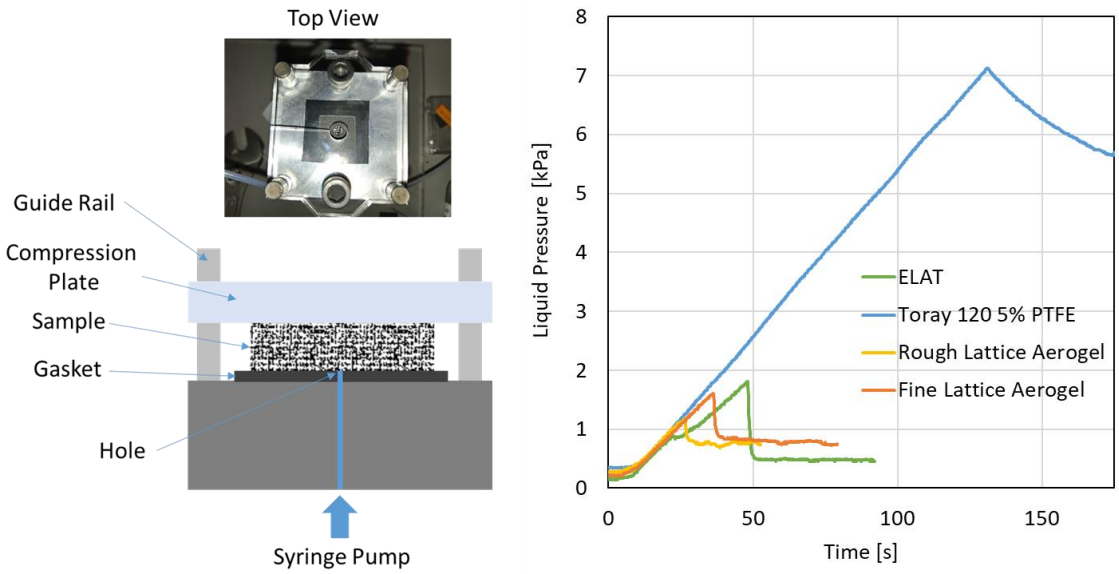

Figure 4. (Left) Injection stage used to measure breakthrough pressure of samples. (Right) Liquid pressure vs. time curves.

Results & Discussion

Breakthrough pressure for each sample is compared in Figure 5. The Toray carbon paper requires the highest breakthrough pressure due to its rigid structure and relatively small pore size. The carbon cloth, which is woven, has larger pores and a flexible structure which provides larger pathways for water transport and thus exhibits lower pressure. The pressure buildup for the ELAT is less steep probably due to the cloth yielding a bit to pressure even when secured in the fixture. Both the CA lattices fall much closer to the ELAT as they have larger liquid specific pathways due to macropores between ligaments. As anticipated, the rough lattice had a lower breakthrough pressure than the fine mesh

due to its increased pore sizes. Comparing the nominal pore diameter to the breakthrough pressure in Figure 5 (Right), a diminishing change in the barrier to drainage is observed for larger pores as predicted by Eq. 1. The sensitivity of breakthrough pressure to changing pore diameters in the lattice structures was ~2.1 Pa/µm. Lattices with smaller gap sizes are of interest for future work to understand the impact of macropores in the lower range. Due to time constraints limited data collection was possible during this proof-of-concept phase and ongoing work will include larger data sets and error analysis.

To explore the tunability of liquid drainage by changing the printed lattice dimensions, Eq. 1 was solved for *r* and a pore diameter was estimated using the measured breakthrough pressure. This technique has been used by prior groups and is of interest because actual pores are not ideal geometries [20]. The estimated pore size gives some idea of the actual geometrical barrier the liquid water interface encounters. Comparing the nominal pore diameters to those calculated from the breakthrough in Figure 6 significant deviation from ideal diameter is observed. The ELAT has the largest deviation, which may be explained by the cloths woven structure. The weave pattern results in larger pores while the fiber bundles contain smaller pores [20]. In this test, since the measured pressure was significantly higher than the literature value of mean pore diameter, the injection path might not have had access to the larger weave pores. For the two 3D printed lattices, the sensitivity of the measured breakthrough pressure pore size to changes in the carbonized pore size is ~0.26 µm/µm and ~0.27 µm/µm when compared to the pre-carbonized printed dimensions. Overall, these early results will inform development going forward.

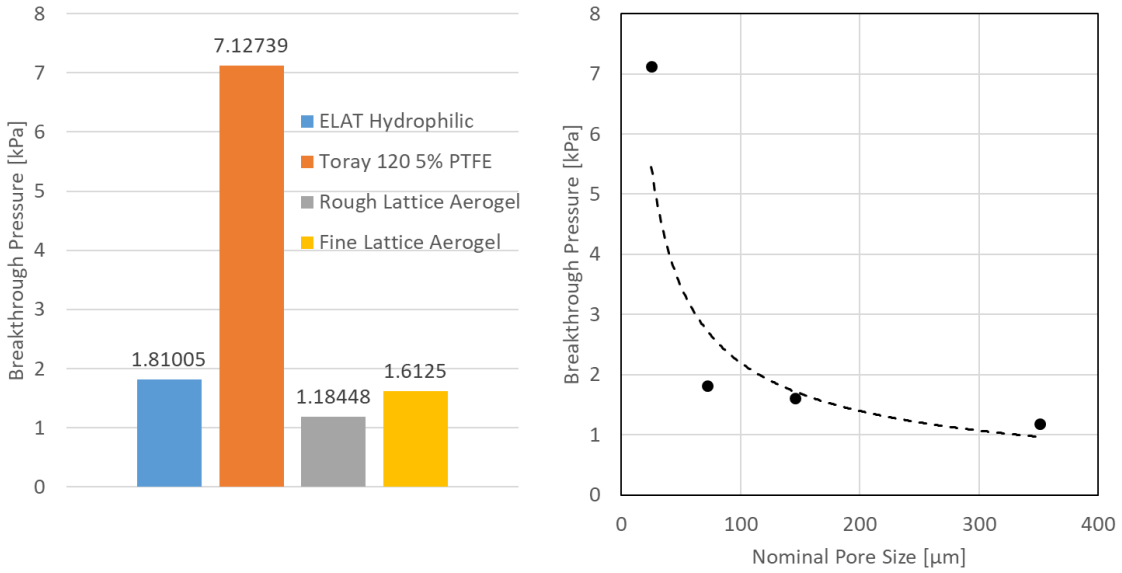

Figure 5. (Left) Breakthrough pressure measured for each sample. (Right) Comparison of breakthrough pressure to nominal pore diameter fit with a power function.

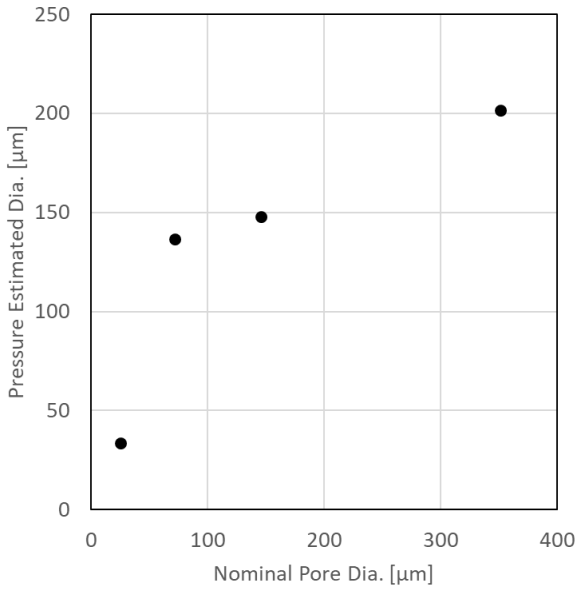

Figure 6. Comparison between nominal pore diameter and diameter estimated from breakthrough pressure and contact angle (Eq. 1).

Consolidated Architectures

3D-printing may enable the consolidation of flow channels and gas-diffusion media as a single structure since channels may be printed directly on top of a base lattice or monolith. Figure 7 (a-c) shows a CA monolith GDL as well as a flow-field/GDL combination. The ability to print channel configurations frees engineers from the limitations of machining and stamping, allowing channel dimensions and geometry to be far more refined for specific transport mechanisms. Non-traditional flow-fields, including porous foams, converging/diverging featured channels, and biomimetic based designs could be better suited to these manufacturing methods. Printing also eliminates the explicit GDL/channel interface. Current PEFC architectures require the flow-field and GDL be compressed together with pressures typically in the range of 2-3 MPa to achieve sufficient electrical conductivity [21]. This compression deforms the GDL causing two primary issues. The first is that the compressive load essentially crushes the carbon fiber under land areas resulting in reduced pore sizes for gas/liquid transport as well as some structural damage. The second issue occurs as these compressive forces cause the GDL to bulge into the flow area; this intrusion has been shown to negatively impact two-phase flow behavior and parasitic pressure drop [22]. 3D-printing gas diffusion media and channels as a single architecture could reduce the need for high compression since high electrical conductivity may now be treated as a design goal for the inherent structure rather than the byproduct of manufacturing methods and material interfaces.

Pore Gradient Lattices

To promote liquid drainage, it may be desirable to print a lattice with increasing pore size from the CL facing GDL side to the channel facing side. This can be accomplished during printing by adjusting the distance between filaments incrementally for each layer in the z-axis. These continually enlarging macropore pathways will provide a mechanism for the capillary driven removal of liquid water while gases can diffuse through the

microporous CA filament structure. Figure 7 (e) shows the backside of a z-axis gradient printed sample. The side facing up is the larger pores which decrease along its thickness and are smallest at the other surface. Since gas can also diffuse through the porous CA filaments, the ability to direct print layers of variable lattice resolution may present new opportunities for MEA design. Such ideas may also be used to improve water removal from land areas where liquid tends to build up due to lack of convective transport [23].

Durability

One challenge to adopting these materials for PEFC applications is improving their strength. MEAs must resist significant levels of compression, vibration, and shock over thousands of hours of operation. Figure 7 (f) shows an example of filament detachment due to liquid surface tension that occurred during a breakthrough test. Incorporating carbon nanotubes (CNT) to form CNT/GA have been shown to improve structural robustness. In early testing, no significant plastic deformation or degradation in compressive strength was observed in CNT/GAs after repeated loading and unloading for up to 10^6 cycles at a strain of 60% [16]. Current work is aimed at these efforts.

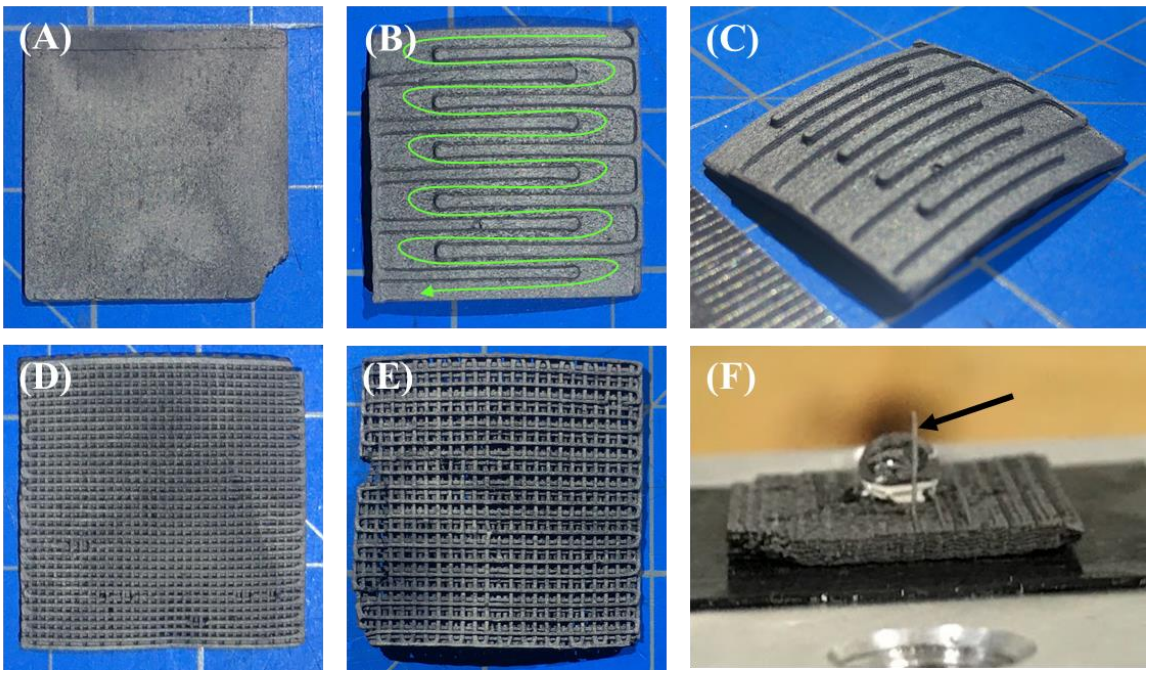

Figure 7. (A) Monolith GDL (B) & (C) Serpentine flow-field channels/GDL single structure print (green arrow is gas flow path) (D) FCC lattice (E) Z-axis pore gradient lattice (F) Ligament detaching from lattice due to surface tension from emerging droplet.

Conclusions

Management of two-phase flow in PEFC MEAs is critical to maintaining their stable and efficient operation. 3D printed CA components, such as GDLs, allow for structured porous media that could enhance PEFC performance by allowing for specific liquid and gas pathways. The overall outcomes of this early exploratory work are:

i.) Graphene based CA GDLs with PEFC applications in mind were 3D printed as rough and fine macropore SCC lattices.
ii.) Breakthrough pressure was measured to be on par with traditional carbon cloth GDL materials.
iii.) Changing the lattice structure dimensions allows for the tuning of breakthrough pressure and liquid drainage.
iv.) Novel structured architectures may be considered using these techniques such as pore gradients and consolidated layers, however, material strength must be improved in the near term.

Acknowledgments

This work was supported by Lawrence Livermore National Laboratory. Dr. Anthony Santamaria was hosted onsite by Dr. Marcus Worsley in the High-Performance Materials group as a part of the LLNL Faculty Mini-Sabbatical Program during summer 2021. This work was performed under the auspices of the U.S. Department of Energy by Lawrence Livermore National Laboratory under contract DE-AC52-07NA27344. Lawrence Livermore National Security, LLC and was supported by LDRD award 20-ERD-019.

References

1. S. Chandrasekaran, M. A. Worsley, A. Meike, *LLNL-TR-830339* (2021)
2. T. Kou, S. Wang, R. Shi, T. Zhang, S. Chiovoloni, J. Q. Lu, W. Chen, M. A. Worsley, B. C. Wood, S. E. Baker, E. B. Duoss, R. Wu, C. Zhu, Y. Li, *Adv. Energy Mater.* **10**, 2002955 (2020)
3. J. Wang, *Appl. Energy* **157**, 640-663 (2015).
4. N.J. Cooper, A.D. Santamaria, M.K. Becton, and J.W. Park, *Energ. Convers. Manage.* **136**, 307-317 (2017).
5. J.P. Owejan, J.J. Gagliardo, J.M. Sergi, S.G. Kandlikar, and T.A. Trabold, *Int. J. Heat Mass Transf.* **49** (25–26), 4721-4731 (2006).
6. M. Glora, M. Wiener, R. Petričević, H. Pröbstle, J. Fricke. *J. Non Cryst. Solids* **285** (1-3) 283-287 (2001)
7. F.Y. Zhang, X.G. Yang, and C.Y. Wang, *J. Electrochem. Soc.* **153** (2), A225-A232 (2006).
8. M. Mortazavi and K. Tajiri, *Renew. Sust. Energ. Rev.*, **45**, 296-317 (2015).
9. A.D. Santamaria, P.K. Das, J.C. MacDonald, and A.Z. Weber, *J. Electrochem. Soc.* **161** (12), F1184 - F1193 (2014).
10. E.F Medici, and J.S. Allen, *J. Pow. Sources*. **191** (2), 417-27 (2009).
11. S. Litster, D. Sinton, N. Djilali, *J. Power Sources*, **154** (1) Pages 95-105 (2006)
12. Z. Lu, J. Waldecker, M. Tam, M. Cimenti, *ECS Transactions*, **69** (17), 1341 (2015)
13. Y. Nagai, J. Eller, T. Hatanaka, S. Yamaguchi, S. Kato, A. Kato, F. Marone, H. Xu, F. N. Büchi, *J. Power Sources*, **435**, 226809 (2019)
14. M. Balakrishnan, P. Shrestha, N. Ge, C. Lee, K. F. Fahy, R. Zeis, V. P. Schulz, B. D. Hatton, A. Bazylak. *ACS Appl. Energy Mater.*, **3** (3) 2695-2707 (2020)
15. D. Niblett, V. Niasar, S. Holmes *J. Electrochem. Soc.***167** (1) 013520 (2019)

16. S. Chandrasekaran, P. G. Campbell, T. F. Baumann, M. A. Worsley, *J. Mater. Res.* **32** (22) 4166-4185 (2017)
17. M. Mortazavi, K. Tajiri. *J. Fuel Cell Sci. Technol.* **11** (2) (2014)
18. S. Park & B. N. Popov, *Fuel* **90**, (1) 436-440 (2011)
19. B. Yao, S. Chandrasekaran, J. Zhang, W. Xiao, F. Qian, C. Zhu, E. B. Duoss, C. M. Spadaccini, M. A. Worsley, Y. Li. *Joule* **3** (2) 459-470 (2019)
20. J. Benziger, J. Nehlsen, D. Blackwell, T. Brennan, J. Itescu. *J. Membr. Sci* **261** (1-2) 98-106 (2005)
21. C. Simon, F. Hasché, H. A. Gasteiger. *J. Electrochem. Soc.* **164** (6) F591 (2017)
22. P. Chippar, O. Kyeongmin, K. Kang, H. Ju. *Int. J. Hydrog. Energy* **37** (7) 6326-6338 (2012)
23. A.D. Santamaria, M.K. Becton, N.J. Cooper, A.Z. Weber, and J.W. Park, *J. Power. Sources*, **293** (20), 162-169 (2015).